Potential and energy of the monoenergetic electrons in an alternative ellipsoid bubble model

R. Sadighi-Bonabi* and SH. Rahmatallahpur
Department of Physics, Sharif University of Technology, 11365-9567 Tehran, Iran
(Received 10 May 2009; revised manuscript received 24 October 2009; published 9 February 2010)

The electron acceleration in the bubble regime is considered during the intense laser-plasma interaction. The presented ellipsoid cavity model is more consistent than the previous spherical model, and it explains the monoenergetic electron trajectory more accurately. At the relativistic region, the maximum energy of electrons in the ellipsoid model is about 24% more than the spherical model, and this is confirmed by PIC and the measured experimental results reported here. The electron energy spectrum is also calculated, and it is found that the energy distribution ratio of electrons $\Delta E/E$ for the ellipsoid model in the here reported condition is about 11% which is less than the one third that of the spherical model. It is in good agreement with the experimentally measured value in the same condition. In this regime, the parameters of the quasi-monoenergetic electrons output beam can be described more appropriately. In this work, 10 TW from 16.6 TW, 500 mJ, and 30-fs laser pulse was focused on the best matched point above a 2-mm-diameter pulsed He gas jet to obtain a stable ellipsoid bubble. Laser intensity of 1.42×10^{19} W cm^{-2} corresponding to a normalized vector potential of $a_0 = 2.6$ focused in a 100-μm^2 spot at the focal point and 1 mm above the edge of the gas jet with an electron density of 1×10^{19} cm^{-3} accelerates electrons to the relativistic velocities. The obtained monoenergetic electron energy spectrum is properly explained by the ellipsoid model introduced here.

DOI: 10.1103/PhysRevA.81.023408 PACS number(s): 52.38.−r, 41.75.Jv, 41.75.Lx, 42.62.−b

I. INTRODUCTION

The continuous rapid advance in the development of relativistic laser systems currently boosts the use of such devices in producing energetic particle beams. Certain types of laser-plasma production of quasi-monoenergetic electrons were predicted and can be explained by the so-called "bubble acceleration" picture [1,2]. In this picture, plasma electrons are expelled off the axis by the front of the incident relativistic laser pulse and form a bubble-like structure with longitudinal and transverse dimensions close to the plasma wavelength λ_p. This bubble is void of electrons at the beginning of the interaction and moves through the background plasma ions with a speed close to the speed of light, c. However, in the frame of the moving bubble, the net positive potential of the bubble core attracts electrons that fall back onto the laser axis behind the cavity. These electrons are captured and accumulated inside the bubble and are thus accelerated to high energies. The energy in the plasma wave could be reabsorbed by the trailing part of the laser pulse when the laser pulse length ($c\tau_L$) is long compared to the electron plasma wavelength. However, if the pulse length is approximately equal or shorter than the plasma wavelength ($c\tau_L \leqslant \lambda_p$), the ponderomotive force excites a wake field with a phase velocity equal to the laser group velocity. Although the generation of monoenergetic electron bunches with distributions of less than 1% and energies above GeV by two laser beam are reported [3], there are main differences between the experimental achievements and theoretical explanation of bubble regime even with a single laser beam. In addition to that, the condition of generating very clean electron beams without any initial Maxwellian branch is under investigation [4–11]. Since the original work of Pukhov and Meyer-ter-Vehn [1], a lot of papers appeared in the literature [4–11]. Thanks to the spherical model of Pukhov and Meyer-ter-Vehn which was an important step forward in the explanation of bubble regime at that time. But the predicted maximum energy of monoenergetic electron bunches was more than two times that of what PIC simulation predicted or experimentally measured [1]. The obvious disagreements of their results with the PIC simulations were acknowledged by themselves [2]. They have explained this controversy as a result of the spherical assumption of the bubble. Some other valuable works were introduced in the general treatment of the "bubble acceleration" and does not give clarification of the electron's energy and its parameters inside the bubble system [11]. Based on the fundamental approach of Pukhov and Meyer-ter-Vehn [1,2], some attempts are made to present a suitable ellipsoidal model and related equations for the energy of the electrons [7,10]. Although some successes were made to improve the prediction of the maximum electron energy, the variation of the electron energy during bubble propagation in the plasma could never be explained properly. In this work, we improved the previous models and resolved the ambiguity in the shape of the potential by correcting equations in the previous elliptical model [10] which were based on the initial spherical model [1,2]. Here we derive a new model and resolve the ambiguity in the shape of the potential. With reproducible equations of the bubble regime, we show that the potential is an ellipsoid. These reliable results correctly explain the effect of the elongation on the variation of the monoenergetic electron energy spectrum. The agreement of the presented model with the experimentally measured parameters and the generation of a very clean electron bunches are also discussed.

II. FIELDS INSIDE RELATIVISTIC ELLIPSOID CAVITY

Imagine a cavity that moves in the plasma. In this regime, the ions are immobile in the cavity while the cavity runs with the relativistic velocity $v_0 \approx 1$ along the x axis. The ion dynamics are neglected because the cavity dimensions are assumed to be smaller than the ion response length, c/ω_{pi},

*sadighi@sharif.ir

where $\omega_{pi} = (4\pi e^2 n_0/M)$ is the ion plasma frequency and M is the ion mass. By writing the Maxwell equations in terms of potentials and using the following convenient gauge, $A_x = -\varphi$, and using a quasistatic approximation by assuming that all quantities depend on $\xi = x - v_0 t$ instead of x and t and using the wake field potential, $\Phi = A_X - \varphi$; instead of the scalar one, we get

$$\Delta\Phi = -\left(\frac{2_0^2}{1+v_0}\right)\frac{\partial}{\partial\xi}(\nabla\cdot A_\perp) + \frac{2}{(1+v_0)^2}\left(1+v_0+v_0^2\right), \tag{1}$$

$$\Delta\Phi = v_0^2\frac{\partial^2}{\partial\xi^2}\Phi + \frac{2}{1+v_0}, \tag{2}$$

$$\Delta A_\perp - v_0^2\frac{\partial^2}{\partial\xi^2}A_\perp = \nabla_\perp\left(\frac{1+v_0}{2}\frac{\partial\Phi}{\partial\xi} + \nabla\cdot A_\perp\right), \tag{3}$$

where inside the cavity we have assumed the electron density n, is zero. We use dimensionless units, normalizing the time to $\omega_p{}^{-1}$, the lengths to c/ω_p, the velocity to c, and the electromagnetic fields to $mc\omega_p/|e|$.

Equations (1) and (3) are similar to the Eqs. (9) and (10), respectively, in Pukhov *et al.* [2]. Based on our calculations, there are some mistakes in the related equations of Pukhov *et al.* [2]. Equation (2) is an essential equation in driving the correct results for spheroid potential and cannot be neglected. The other fundamental error is in the coefficients of Eqs. (1) and (3) which we have corrected it. Compare Eqs. (1) and (3) with $v_0 = 1$, with Eqs. (9) and (10) of Ref. [2]. In the following, a reliable calculation is presented which is in good agreements with PIC simulation and the experimental data. From Eqs. (1) and (2), we have

$$\nabla_\perp\cdot A_\perp = -\frac{1+v_0}{2}\frac{\partial}{\partial\xi}\Phi + \frac{1}{1+v_0}\xi. \tag{4}$$

Substituting above equation in Eq. (3), we get

$$\Delta A_\perp - v_0^2\frac{\partial^2}{\partial\xi^2}A_\perp = 0. \tag{5}$$

And from Eq. (2), we have

$$\Delta_\perp\Phi + \left(1-v_0^2\right)\frac{\partial^2}{\partial\xi^2}\Phi = \frac{2}{1+v_0}, \tag{6}$$

where $\Delta_\perp\Phi = \frac{\partial^2}{\partial y^2}\Phi + \frac{\partial^2}{\partial z^2}\Phi$.

By assuming the dependency of ϕ on ξ, y, z is $\phi = \phi_1(\xi) + \phi_2(y,z)$, and by substituting it in Eq. (6), we can get $\Delta_\perp\Phi_2 + (1-v_0^2)\frac{\partial^2}{\partial\xi^2}\Phi_1 = \frac{2}{1+v_0}$. The first term depend on y and z, while the second term depends on ξ. Therefore, we can solve this equation with the separations of variables and set those equal to a parameter c independent of ξ, y, z, where it can depend on v_o, plasma parameter ω_p, and laser parameters a_o and w_o as $c = c(v_0, \omega_p, a_0, w_0)$. Remembering that c is independent of ξ, y, z since $(v_0, \omega_p, a_0, w_0)$ are independent of the above-mentioned variables. Then we have

$$\Delta_\perp\Phi_2 = c. \tag{7}$$

By substituting Eq. (7) in Eq. (6), we get

$$\left(1-v_0^2\right)\frac{\partial^2}{\partial\xi^2}\Phi_1 = \frac{2}{1+v_0} - c. \tag{8}$$

As seen from Eq. (8), if we let $v_0 = 1$, then $c = 1$ and the dependency of potential on the component ξ disappears completely; in this case, the solution of Eqs. (7) and (8) is

$$\Phi(\xi, y, z) = \frac{y^2}{4} + \frac{z^2}{4} + \phi_1(\xi), \tag{9}$$

where $\phi_1(\xi)$ can be any kind of function, In another word, from Eq. (9), one cannot reach a spherical potential for $\Phi(\xi, y, z)$, unless assuming that there is a spherical potential as they did in Ref. [2]. Therefore, by preferring and assuming a priority to have a spherical potential, we can reach to the spherical potential of Pukhov *et al.* from Eq. (9) as follows:

$$\phi_1(\xi) = \frac{\xi^2}{4}, \quad \Phi(\xi, y, z) = \frac{y^2}{4} + \frac{z^2}{4} + \frac{\xi^2}{4}.$$

But we always have $v_0 < 1$, only in the limit one can arbitrarily reach to $v_0 = 1$; then from Eq. (8), we have

$$\begin{aligned}\phi_1(\xi) &= \frac{1}{1-v_0^2}\left(\frac{2}{1+v_0} - c\right)\frac{\xi^2}{2} \\ &= \frac{1}{1-v_0^2}\left(\frac{2-c-v_0c}{1+v_0}\right)\frac{\xi^2}{2} \\ &= \frac{1}{(1+v_0)^2}\left(\frac{2-c-v_0c}{1-v_0}\right)\frac{\xi^2}{2}.\end{aligned} \tag{10}$$

By principal of continuity and in the limit of $v_0 \to 1$, we get

$$\phi_1(\xi) = \frac{(c+2c')\xi^2}{8}. \tag{11}$$

Here for simplicity, we set $c = c(v_0, \omega_p, a_0, w_0)$ and $c' = \frac{\partial}{\partial v_0}c(v_0, \omega_p, a_0, w_0)$; the solution of Eq. (7) is $\phi_2(\xi, y, z) = c(\frac{y^2}{4} + \frac{z^2}{4})$, and from Eq. (11), we have

$$\Phi(\xi, y, z) = \frac{(c+2c')\xi^2}{8} + c\frac{y^2}{4} + c\frac{z^2}{4}.$$

Then by substituting Eq. (11) in the Eq. (4), we get

$$\nabla_\perp\cdot A_\perp = \frac{2-c-2c'}{4}\xi. \tag{12}$$

Since we have symmetry in y and z directions, so we can choose $\frac{\partial}{\partial y}A_y = \frac{\partial}{\partial z}A_z = \frac{2-c-2c'}{8}\xi A$; the solution satisfying Eq. (5) with the above condition is $A_\perp = (\frac{2-c-2c'}{8}y\xi, \ \frac{2-c-2c'}{8}z\xi)$. Therefore, we have

$$\Phi(\xi, y, z) = 1 + \left[\frac{(c+2c')\xi^2}{8} + c\frac{y^2}{4} + c\frac{z^2}{4} - \phi_0\right], \tag{13}$$

$$A = (A_x, A_\perp) = \left(\frac{\Phi}{2}, \frac{2-c-2c'}{8}y\xi, \frac{2-c-2c'}{8}z\xi\right). \tag{14}$$

The integration constant ϕ_0 is chosen such that on the surface of the ellipsoid $\Phi = 1$. The ϕ dependency on ξ, y, z is almost quadratic, but their coefficients are not necessarily equal. If we prefer to have a spherical solution, we should choose c such that $(c+2c')/8 = c/4$.

In Fig. 1, the electron trajectory is plotted from a fully nonlinear particle in cell (XOOPIC) simulation according to here presented experimental conditions [$w_0 = 5.5$ μm,

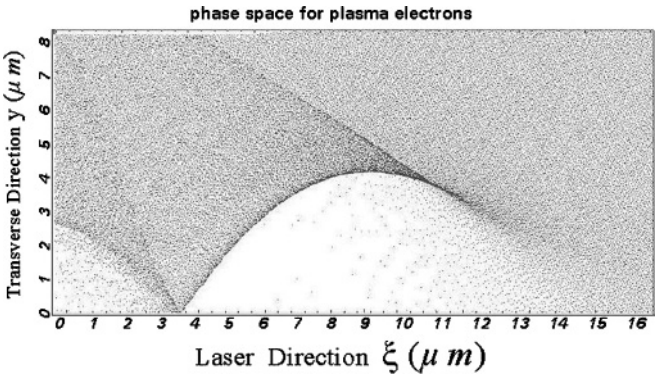

FIG. 1. The electron trajectory in the bubble regime produced in a uniform plasma cavity, simulated by XOOPIC, in condition of the here mentioned experiment. The elongation in the z direction is evident, and the dimensions of bubble are not equal, which confirms the shape of bubbles are ellipsoid instead of sphere (dimensions are not scaled).

$a_0 = 2.6$, $\lambda_p = 11$ μm], where we get $R_e = 4$ μm. From this figure, it is evident that the dimensions of bubble are not equal and we have elongation in the z direction.

Figure 2 indicates a typical electron trajectory for the spherical and ellipsoidal potentials in the ξ, y plane for the same initial conditions. In this figure, the trajectory elongation in the direction of ξ for the ellipsoid potential is shown.

III. ENERGY OF ELECTRONS

The energy of electrons in an ellipsoid cavity can be derived by using the Hamiltonian formulation [2].

$$H = \sqrt{1+p^2+a^2} - v_0 p + (1+v_0)\Phi/2 \approx \gamma - p + \Phi,$$

where p is the momentum, a is the normalized vector potential of the laser field, and γ is the electron energy, and we have used the wake potential Φ.

Reformulating Eq. (13) as follows:

$$\Phi(\xi, y, z) = 1 + \phi_0\left(\frac{\xi^2}{a_e^2} + \frac{y^2}{b_e^2} + \frac{z^2}{b_e^2} - 1\right), \qquad \frac{\phi_0}{a_e^2} = \frac{(c+2c')}{8}, \quad \frac{\phi_0}{b_e^2} = \frac{c}{4}. \tag{15}$$

We have $\gamma \approx 2\gamma_0^2[1 + \phi_0(1 - \frac{\xi^2}{a_e^2})] \approx 2\gamma_0^2\phi_0(1 - \frac{\xi^2}{a_e^2})$.

The maximum energy of the accelerated electrons in a spheroid peaks at the cavity center of

$$\gamma_{\max} \approx 2\gamma_0^2\phi_0 = \gamma_0^2\frac{(c+2c')a_e^2}{4} = \gamma_0^2\frac{cb_e^2}{2}. \tag{16}$$

In order to compare the spheroid model with the spherical model, let $c' = 0$ and consider a spherical bubble with radius R, let

$$a_e b_e^2 = R^3, \tag{17}$$

where a_e and b_e are the axis of spheroid; in this case, spheroid and sphere have equal volume and charge density (let $a_e = b_e = R$), we have

$$\gamma_{\text{maxsphere}} \approx \gamma_0^2 R^2/2. \tag{18}$$

Comparing Eqs. (16), (17), and (18), we see that $\gamma_{\max} \leqslant \gamma_{\text{maxsphere}}$.

In other words, the maximum energy of the spheroid model is less than the spherical model and it is close to the PIC simulations [2] (see Fig. 8). From Ref. [12], we have $\gamma = \gamma_0(1+\gamma_0)\Delta\varphi \pm \gamma_0 v_0\sqrt{(1+\gamma_0\Delta\varphi)^2 - 1}$, where φ is the scalar potential, $\Delta\varphi = \varphi_{\max} - \varphi_{\min}$, and $\pm$ give $\gamma_{\max}$ and $\gamma_{\min}$.

For an ultra-high intense laser pulse, we have $\gamma_0\Delta\varphi \gg 1$, by defining $\Delta\gamma$ as the difference between $\gamma_{\max}$ and $\gamma_{\min}$; from the above equation, we have

$$\Delta\gamma = \gamma_{\max} - \gamma_{\min} = 2v_0\gamma_0\sqrt{(1+\gamma_0\Delta\varphi)^2 - 1} \approx 2\gamma_0^2\Delta\varphi;$$

for the spherical model, we have $\Delta\varphi_{\text{sphere}} \approx R^2/4$, and for the spheroid model, we have $\Delta\varphi \approx \phi_0$. From Eqs. (15) and (17), we always have $\Delta\varphi \leqslant \Delta\varphi_{\text{sphere}}$ or $\Delta\gamma \leqslant \Delta\gamma_{\text{sphere}}$. So in the spheroid cavity model, the electron energy has a narrow spread spectrum in comparison to the spherical model which is in better agreement with the experimental data as shown in Fig. 8.

At the beginning of our interaction of the laser pulse with plasma, the bubble shape is determined by the ponderomotive force of the laser pulse. The electrons form a narrow sheath surf tangentially to the bubble boundary, and at the middle of the bubble where we have a return current, the transverse force

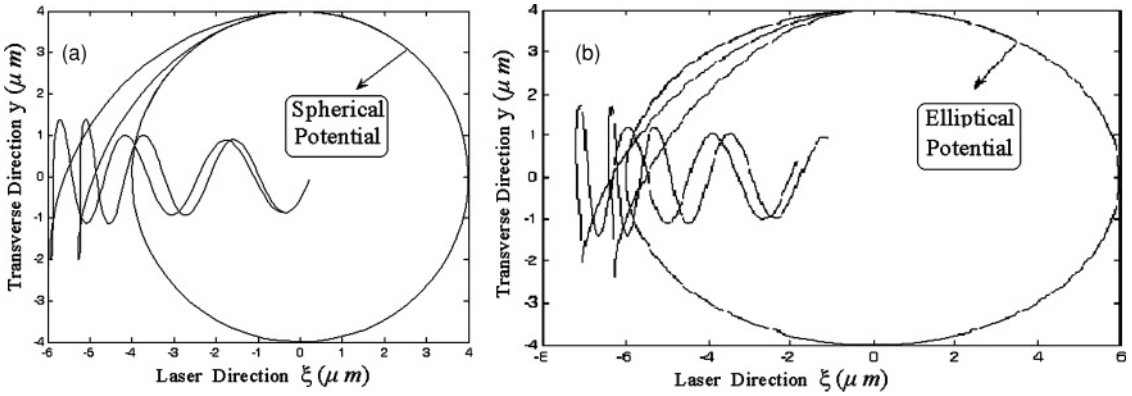

FIG. 2. The typical electron trajectory. (a) Spherical model. (b) Ellipsoid potential in the (ξ, y) plane. The electrons with the specified energy can enter the bubble in both regimes.

is zero. In this condition, we have [2]

$$\frac{cR_e}{4}(1+v_x) \approx \frac{cR_e}{4} \approx \nabla_\perp \sqrt{1+a^2}, \tag{19}$$

where R_e is the transverse bubble radius and the laser pulse is written for a circularly polarized with amplitude (a) focused to a spot size of w_0 with a Gaussian profile as $a = a_0 \exp[-(y^2 + z^2)/2w_0^2]$; for simplicity, we have set $v_0 = 1$ and $v_x = 0$. The transverse bubble radius can be determined from [13] as

$$R_e \approx w_0 \sqrt{\ln\left(\frac{\lambda_p a_0}{\sqrt{c\pi w_0}}\right)} \tag{20}$$

or

$$c = \frac{\lambda_p^2}{\pi^2 w_0^2} a_0^2 \exp\left(-2R_e^2/w_0^2\right). \tag{21}$$

Therefore, c is proportional to the normalized laser intensity a_0 and inversely to the laser spot size w_0 . These equations apparently show that by increasing the laser intensity or decreasing the spot size, the parameter c increases. For our experiment by focusing 60% of 16.6-TW laser power (10 TW) into a spot with the area of 100 μm^2 ($w_0 = 5.5$ μm), we have $a_0 = 2.6$ and $\lambda_p = 11$ μm and we get $R_e = 4$ μm.

From the area under curves of Fig. 8 we can calculate the amount of accelerated electrons which is representing $N_e E_e$. Form experimental curve this amount for the share of monoenergetic electrons is 7.5×10^{10} electrons MeV sr. By considering the same amount for ellipsoidal and for spherical models and by using the related maximum amounts for their related curves are plotted in Fig. 8. The achieved distributions for the electrons are discussed in the next section.

IV. EXPERIMENTAL RESULT

In Fig. 3, the schematic overview of the experimental setup used here is given. The experiment was carried out by a 500-mJ, 30-fs Ti:sapphire chirped pulse amplification laser system to generate a laser acceleration wake field to generate monoenergetic electron bunches. The spot size from the pulse compressor was 1.38 cm^2 with a center wavelength of 800 nm, where it is focused onto a supersonic He gas jet by an off-axis mirror. The position of other elements such as a CCD camera and electron microscope also indicated. Some descriptions of experimental arrangement were given in our earlier work [10].

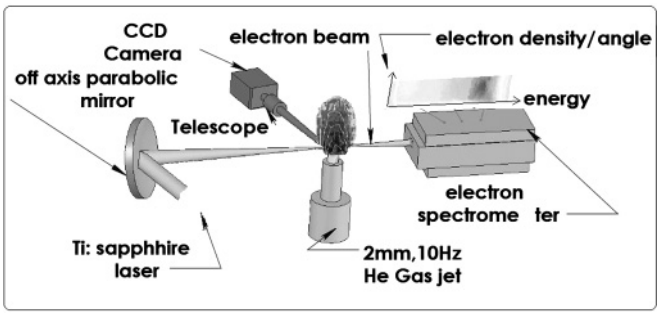

FIG. 3. Experimental setup for producing monoenergetic electron bunches. The path of the laser beam and the position of the basic instruments such as a helium gas jet, a CCD optical camera, an off-axis mirror, and an electron spectrometer are shown.

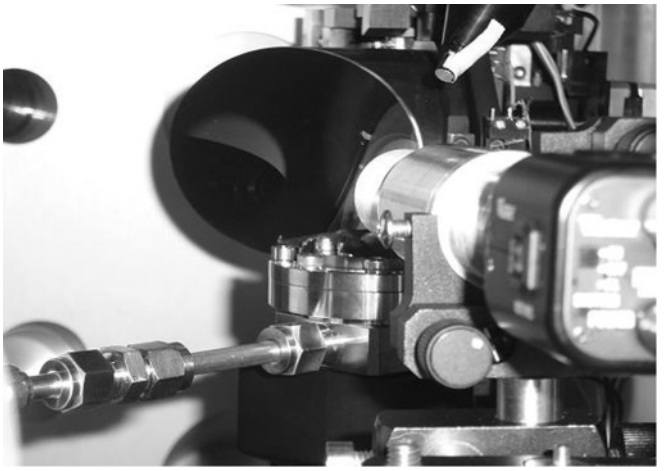

FIG. 4. Picture from inside of the laser interaction area of the intense laser with the He gas jet. The off-axes mirror which was used to focus laser beams with the waist of 1.38 cm^2 at a 100-μm^2 spot at the tip of the nozzle is shown.

Here we describe the laser parameters and diagnostics in more detail. In Fig. 4, a picture from the inside of a vacuum chamber, including $f/5$ off-axes mirror (OAM), and the position of the gas jet exit is shown. The gold-coated parabolic mirror focuses the 166-TW laser pulse in a spot of 100 μm^2 at the edge of 10-Hz gas jet where it contains about 60% of the laser intensity corresponding to the intensity of 1.42×10^{19} W cm^{-2} at the focusing point in the gas jet. In order to have a consistent target condition for each laser shot, a new target material is required. Since the relativistic electrons are produced within a distance of few hundred micrometers producing and measuring of the specific gas density profile is an essential problem. This is provided by interferometers by measuring the phase shift [13–15]. By using a pulsed laser, time transit information about the gas density which directly depends on the gas pressure is obtained. When a fast high voltage opens the gas valve, the gas pressure linearly increased and following the gas expansion slowly decreases. The high-intensity short laser pulse is synchronously fired at the moment of highest pressure. Therefore, both have the same repetition rate which was 10 Hz in the present work. Here a supersonic gas jet was made by a cylindrical capillary nozzle with an inner diameter of 2 mm connected to a gas valve at high pressures. The gas density distribution on the nozzle tip is indicated in Fig. 5. The vertical color code represents the two-dimensional pressure distribution of He gas up to 2.8×10^{20} cm^{-3} on the nozzle center at 1 mm above the exit. At this condition, the filing pressure of the gas valve was above 10 bars. In Fig. 6, the picture of the focused spot of the laser pulse is shown which was set at the tip of the gas nozzle and 1 mm above the gas jet exit. The spot diameters were 11 μm horizontally and 12 μm vertically at full width at half maximum in vacuum. and contains 60% of the 16.6 TW of the focused laser power resulting in an intensity of 1.42×10^{19} W cm^{-2} with the power of about 10 TW at the focal spot corresponding to a $a_0 = 2.6$ normalized vector potential.

The energy spectrum of the accelerated electrons was measured using an electron spectrometer with a permanent magnet. The electron spectrometer was placed in the

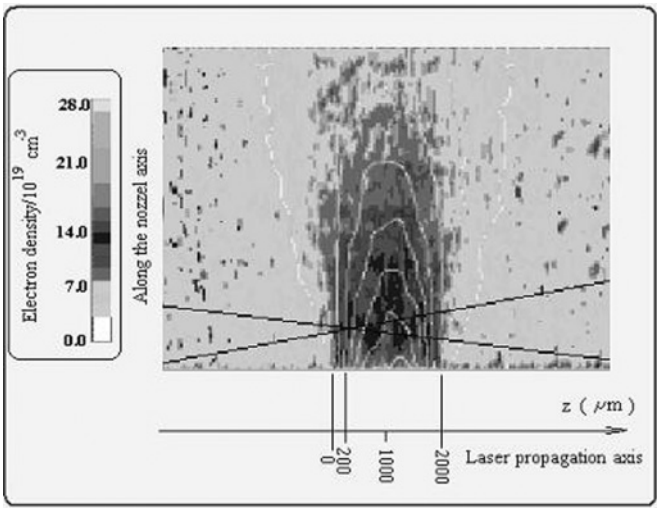

FIG. 5. The lateral Gaussian density profile (z direction) of electrons above the gas nozzle. The 2-mm-diameter, high-pressure He gas jet produces the initial electron density of up to 2.8×10^{20} cm^{-3}. The vertical color code to the left indicates the electron density which is linearly proportional to the gas pressure.

z direction and makes use of the electron deflection in a magnetic field, and the measured energy range was from 0.1 to 100 MeV and recorded on image plates from Fuji Film covered with 15-μm-thick Al foil to prevent exposure by scattered laser light and stop low-energy electrons. The image plates placed off axis to avoid affecting other produced radiations such as γ rays and X rays on their surfaces. The housing of the electron spectrometer was shielded with high Z materials to prevent the detection of unwanted radiations and ensure only desired produced electrons were detected.

By consideration of the self-modulated laser wake-field acceleration (SMLWFA), $c\tau = nR_e$ is the most stable cavity condition [13,14]. So the stable condition can be obtained for $R_e = m\lambda_p/2$, where n and m are positive integer numbers. By focusing the laser beam at different positions from the beginning of the gas jet, we obtained various electron energy

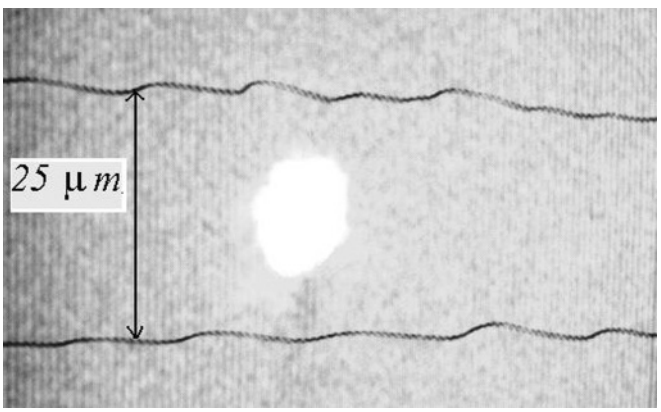

FIG. 6. Laser beam waist (diameter) at focus is shown at 1 mm above the gas jet which was 11 μm horizontally and 12 μm vertically resulting in vacuum contains 60% of the laser intensity results to focused intensity of 1.42×10^{19} W cm^{-2} corresponding to a normalized vector potential of $a_0 = 2.6$.

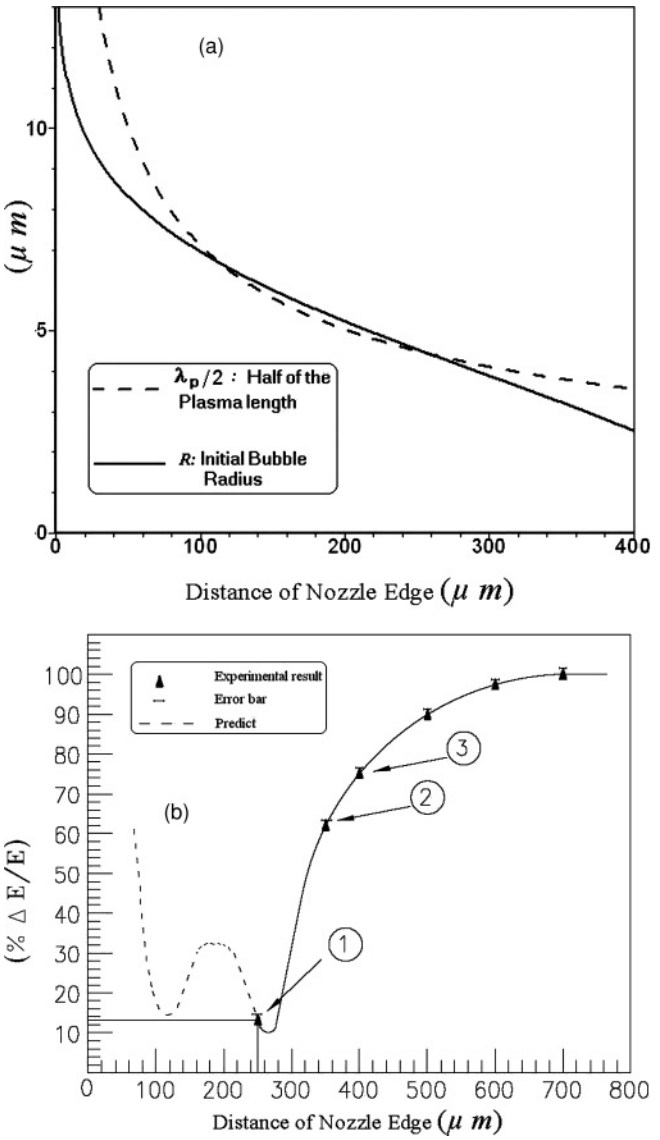

FIG. 7. Scanning the laser pulse along the gas jet exit: (a) The intersection points of $\lambda_p(z)/2$ and $R(z)$ are the optimum points to produce stable bubbles to trap monoenergetic electrons. (b) Electron energy distribution $\Delta E/E$. The maximum electron plasma density was 1.4×10^{20} cm^{-3}. The dashed part is plotted from the predicted parameters of Fig. 7(a).

profiles. Most of the electron energy spectrums possess a Maxwellian or mixed with quasi-monoenergetic distribution. In this experiment, we did not observe any evidence of bubble formation resulting in monoenergetic electrons up to 200 ± 5 μm from the beginning of the gas jet. Figure 7(a) shows that one can obtain high-energy electrons with narrower energy distribution by better and precise focusing. At 200 ± 5 μm [at point 1 of Fig. 7(b)], we obtained quasi-monoenergetic electrons which are shown in Fig. 8. We can conclude from Fig. 7(a) that the point 1 of Fig. 7(b) corresponds to the bubble radius of only 4 μm, which is smaller than our 5.5-μm spot size radius. However, the first minimum point in Fig. 7(b) corresponds to a bubble radius larger than 6.5 μm. Thus, we were not able to detect this point with our 5.5-μm laser beam spot size radius. When we moved further along the

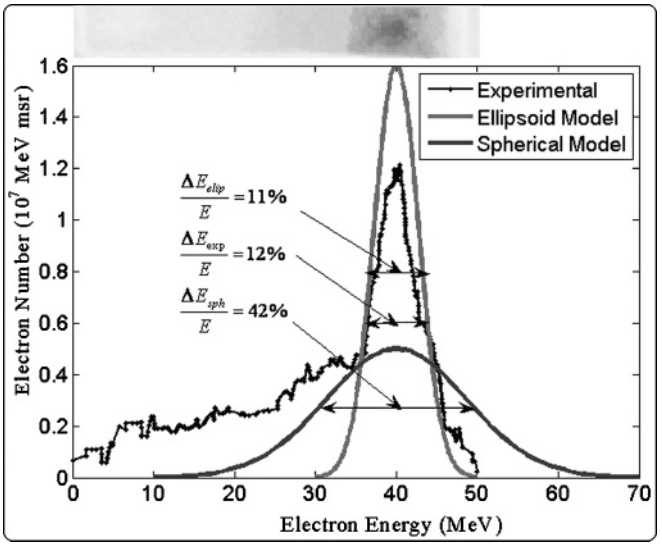

FIG. 8. Comparing of here derived ellipsoidal models with the spherical model and measured experimental result in the same condition. The maximum energy and related electron energy distribution of ellipsoid model in comparison to the spherical model is in much better agreement with the experimental measurements. The image plate for monoenergetic electrons related to point 1 of Fig. 7(b) is also presented.

laser beam, the profile of the electrons changed more to the quasi-Maxwellian shapes [points 2 and 3 of Fig. 7(b)]. Under the conditions of this experiment (focusing radius of 5.5 μm), points more than 600 μm showed 100% distribution of electron energy as we can see in Fig. 7(b). In experiments, monoenergetic electron bunches only can be observed in a very narrow window of plasma, target, and laser parameters where in a specific density profile, only specific points with a defined laser pulse duration as well as a focusing ratio can produce monoenergetic electron beams. The accuracy of the focusing device is another sensitive point in this work. By better focusing around the minimum point at about 270 μm which was not possible because of instrumental limitations [see Fig. 7(b)], quasi-monoenergetic electrons bunches with much lower distributions can be produced. In order to observe bigger bubbles for trapping more electrons, one has to use laser beams with higher powers or compress the initial laser pulses to shorter pulse durations to obtain larger focal spots with intensities larger than the critical relativistic intensities. However, at the first minimum, by producing a larger bubble due to dependence of electron energy to the bubble radius, the energy distribution of the electrons is increased.

When approaching the minimum of the crossing points of Fig. 7(a), the electron beam becomes more monoenergetic. Therefore, when the laser beam is focused in the best matched point in the edge of the gas jet, then the background Maxwellian electrons are canceled. For producing more monoenergetic electrons, we have focused the laser beam to the second minimum of the Fig. 7(a). Very fine tuning is required for obtaining a very clean mono-energetic electron bunches without any lower energy electrons outside the bubbles with mixed Maxwellian distribution. In Fig. 8, we compared the measured monoenergetic electron pulse energy spectrum with the results predicted from a here mentioned ellipsoid model and the spherical model with the same total energy (see Fig. 8). As we can see, the ellipsoid cavity holds the electron bunch in the quasi-monoenergetic regime better than the previous spherical cavity. From Fig. 8, we can see the maximum energy of the here presented model about 24% lower than the earlier spherical model which is in good agreement with the here measured experimental amounts. In this figure, also the related image plate to the electron spectrum produced at 250 μm [point 1 of Fig. 7)] is presented.

V. CONCLUSIONS

In the present work, we derived a reliable analytical expression for the potential within a cavity moving at relativistic velocity in plasma. We have improved the previous model when the bubble velocities are approaching the velocity of light, and we showed that in fact in these conditions, the potentials are in the ellipsoidal shape. We also derived the maximum energy of the electrons and the electron energy spectrum and found that the maximum energy in the ellipsoid model is considerably less than that in the spherical model and very close to the experimental values and reported PIC simulations [2]. In the experimental part of this work, we have focused the laser pulse in the best matched point above the nozzle gas exit to obtain a stable ellipsoid bubble. The relative energy distributions of the experimentally produced electrons with $\Delta E/E = 12$ (see Fig. 8) was less than one third of previous spherical model (42%) which is in excellent agreement with the here presented ellipsoidal model with only $\Delta E/E = 11$ in the experimental conditions presented here.

ACKNOWLEDGMENTS

The authors acknowledge the Ministry of Oil (IRI) for partial support of this work through Contract No. 121 by the Pars Oil and Gas Company, as well as the support by the Research Deputy Office at the Sharif University of Technology. We deeply appreciate Prof. J. Zhang and his team for their experimental help and P. Zobdeh, as well as the constructive comments of Prof. Malka at the Kathmandu Conference.

[1] A. Pukhov and J. Meyer-ter-Vehn, Appl. Phys. B: Lasers Opt. **74**, 355 (2002).

[2] I. Kostyukov, A. Pukhov, and S. Kiselev, Phys. Plasmas **11**, 5256 (2004).

[3] C. Rechatin, J. Faure, A. Ben-Ismail, J. Lim, R. Fitour, A. Specka, H. Videau, A. Tafzi, and V. Malka, Phys. Rev. Lett. **102**, 164801 (2009).

[4] S. P. D. Mangles, C. D. Murphy, Z. Najmudin, A. G. R. Thomas, J. L. Collier, A. E. Dangor, E. J. Divall, P. S. Foster, J. G. Gallacher, C. J. Hooker, D. A. Jaroszynski, A. J. Langley, W. B. Mori, P. A. Norreys, F. S. Tsung, R. Viskup, B. R. Walton, and K. Krushelnick, Nature (London) **431**, 535 (2004).

[5] C. G. R. Geddes, Cs. Toth, J. van Tilborg, E. H. Esarey, C. B. Schroeder, D. Bruhwiler, C. Nieter, J. Cary, and W. P. Leemans, Nature (London) **431**, 538 (2004).

[6] J. Faure, Y. Glinec, A. Pukhov, S. Kiselev, S. Gordienko, E. Lefebvre, J.-P. Rousseau, F. Burgy, and V. Malka, Nature (London) **431**, 541 (2004).

[7] R. Sadighi-Bonabi, S. Rahmatallahpor, H. A. Navid, E. Lotfi, P. Zobdeh, Z. Reiazie, M. Bostan-doust, and M. Mohamadian, Contrib. Plasma Phys. **49**, 49 (2009).

[8] K. Nemeth, B. Shen, Y. Li, H. Shang, R. Crowell, K. C. Harkay, and J. R. Cary, Phys. Rev. Lett. **100**, 095002 (2008).

[9] S. P. D. Mangles, Phys. Rev. Lett. **96**, 215001 (2006).

[10] R. Sadighi-Bonabi, H. A. Navid, and P. Zobdeh, Laser Part. Beams **27**, 223 (2009).

[11] W. Lu, C. Huang, M. Zhou, W. B. Mori, and T. Katsouleas, Phys. Rev. Lett. **96**, 165002 (2006).

[12] E. Esarey and M. Pilloff, Phys. Plasmas **2** (5), 1432, (1995).

[13] B. Hidding, K. U. Amthor, B. Liesfeld, H. Schwoerer, S. Karsch, M. Geissler, L. Veisz, K. Schmid, J. G. Gallacher, S. P. Jamison, D. Jaroszynski, G. Pretzler, and R. Sauerbrey, Phys. Rev. Lett. **96**, 105004 (2006).

[14] K. U. Amthor, Laser plasma accelerators for charged particles, Ph.D. thesis, Friedrich-Schiller-University Jena, 2006.

[15] R. Benattar, C. Popovics, and R. Sigel, Rev. Sci. Instrum. **50**, 1583 (1979).